

CONTINUOUS EDDY SIMULATION (CES): CONCEPTUAL APPROACH AND APPLICATIONS

Stefan Heinz

Department of Mathematics & Statistics
University of Wyoming
1000 E. Univ. Ave., Laramie, WY 82071, USA
heinz@uwyo.edu

Adeyemi Fagbade

Department of Mathematics & Statistics
University of Wyoming
1000 E. Univ. Ave., Laramie, WY 82071, USA
afagbade@uwyo.edu

ABSTRACT

The simulation of high Reynolds number (Re) separated turbulent flows faces significant problems for decades: large eddy simulation (LES) is computationally too expensive, and Reynolds-averaged Navier-Stokes (RANS) methods and hybrid RANS-LES methods often provide unreliable results. This has serious consequences, we are currently unable to reliably predict very high Re regimes, which hampers applications and our understanding of turbulence structures. The paper reports the advantages of a strict mathematical approach, continuous eddy simulation (CES), to derive partially resolving turbulence models. In contrast to popular hybrid RANS-LES, this minimal error approach includes a dynamic modification of the turbulence model in response to the actual flow resolution: the model can increase (decrease) its contribution to the simulation in dependence of a low (high) flow resolution. This property is the essential requirement to seamlessly cover RANS and LES regimes. The CES modeling approach offers essential advantages regarding its functionality: basically, it is independent of a variety of simulation settings applied in popular hybrid RANS-LES to improve the model performance. In addition, the CES computational cost can be below the cost of other hybrid RANS-LES and LES by orders of magnitude. Essential simulation performance advantages of CES simulations are described here with respect to three complex flow applications: periodic hill flows at high Reynolds number (Heinz *et al.*, 2020), the NASA wall-mounted hump flow (Seifert & Pack, 2002), and the Bachalo & Johnson axisymmetric transonic hump flow (Bachalo & Johnson, 1986; Lynch *et al.*, 2020).

INTRODUCTION

Turbulent flows of practical relevance are often characterized by a high Re and (depending on the flow geometry) flow separation. It is well-known that reliable and efficient simulations of separated high Re turbulent flows face significant problems. Reynolds-averaged Navier-Stokes (RANS) methods are known to be often unreliable. Large eddy simulation (LES) is aiming at a realistic simulation of instantaneous turbulence, but LES is limited to not too high Re flow simulations because of significant computational cost requirements.

The most appropriate balance between RANS and LES approaches is the design of hybrid RANS-LES methods (Heinz, 2020; Menter *et al.*, 2021). A large variety of such hybrid RANS-LES was introduced so far. The problem of these hybrid RANS-LES is their limited reliability: there

is a lack of proven predictive power, all such hybrid RANS-LES results need validation, which is often hardly possible. For example, a usual problem of popular hybrid RANS-LES, wall-modeled LES (WMLES) (Larsson *et al.*, 2016) and detached eddy simulation (DES) methods (Mockett *et al.*, 2012), is the significant uncertainty of predictions depending on adjustable model settings. Such predictions depend on different (equilibrium, nonequilibrium) wall models applied, definitions of regions where different models and grids are applied, different mesh distributions, and set-up options to manage the data transfer between such different flow regions (Heinz, 2020).

An explanation for the problems faced by popular hybrid RANS-LES provides the concept of these methods to generate conditions which enable the model to produce as much as possible resolved motion. This idea does not ensure at all a physically meaningful simulation. The best example is LES performed on coarse grids. Although there is a lot of resolved motion, such simulations are known to usually provide unphysical results. It is plausible that the uncontrolled balance between modeled motion represented by the model and produced resolved motion implies the sensitive dependence of model results on changes of simulation settings (see the discussion in the preceding paragraph). The most relevant problem is that usually applied hybrid RANS-LES do not enable a seamless transition between RANS and LES regimes. For example, simulations of the effect of increasing Re using the same grid face a decrease of the amount of resolved motion. The model needs to compensate this loss of total kinetic energy by increasing its contribution to the simulation. In general, a functional RANS-LES swing requires that the model contribution to the simulation is relatively low (high) if the flow resolution is high (low). The latter requires that the model receives information about the amount of resolved motion, which is not the case in regard to usually applied hybrid RANS-LES.

These issues lead to the question of which more appropriate simulation concepts can be applied to overcome these serious problems. The most promising approach is the design of a computational method that minimizes the hybridization error: the expectation is that a minimal error requires an appropriate balance of resolved and modeled motion. Such methods [continuous eddy simulation (CES) methods] were introduced recently: see Refs. (Heinz, 2019; Heinz *et al.*, 2020; Heinz, 2021, 2022; Fagbade & Heinz, 2024*a,b*). The motivation for presenting this paper is to describe the main characteristics of CES methods in conjunction with their ability to overcome the issues of popular hybrid RANS-LES.

$\frac{Dk}{Dt} = P - \varepsilon + D_k, \quad \frac{D\omega}{Dt} = C_{\omega_1} \omega^2 \left(\frac{P}{\varepsilon} - \beta^* \right) + D_{\omega}, \quad D_k = \frac{\partial}{\partial x_j} v_t^* \frac{\partial k}{\partial x_j}, \quad D_{\omega} = \frac{\partial}{\partial x_j} v_t^* \sigma_{\omega} \frac{\partial \omega}{\partial x_j}$	(KOS)
$\frac{Dk}{Dt} = P - \psi_{\beta} \varepsilon + D_k, \quad \frac{D\omega}{Dt} = C_{\omega_1} \omega^2 \left(\frac{P}{\varepsilon} - \beta \right) + D_{\omega}, \quad \beta^* = 1 + \beta - \psi_{\beta}$	(KOK)

<ul style="list-style-type: none"> Analysis option \mathcal{O}_1 [with $Dk/Dt, D\omega/Dt, v_t^* = v_{t, tot}$]: $\left[\frac{\delta(Dk/Dt)}{Dk/Dt} = \frac{\delta D_k}{D_k} = \frac{\delta k}{k}, \quad \frac{\delta(D\omega/Dt)}{D\omega/Dt} = \frac{\delta D_{\omega}}{D_{\omega}} = \frac{\delta \omega}{\omega} \right]$ $\lambda_1 = C_{\omega_1} \omega^2 \left(\frac{P}{\varepsilon} - \beta_1^* \right) + D_{\omega} - \frac{D\omega}{Dt}, \quad \delta \left(\frac{\lambda_1}{\omega} \right) = \frac{C_{\omega_1}}{\tau} (\beta_1^* - 1) \left[\frac{\delta \tau}{\tau} - \frac{\delta \beta_1^*}{\beta_1^* - 1} \right], \quad \int_{\beta}^{\beta_1^*} \frac{dx}{x-1} = \int_{\tau_{tot}}^{\tau} \frac{dy}{y}, \quad \frac{\beta_1^* - 1}{\beta - 1} = \tau_+$
<ul style="list-style-type: none"> Analysis option \mathcal{O}_2 [without $Dk/Dt, D\omega/Dt, v_t^* = v_t$]: $\left[\delta D_k/D_k = 3\delta k/k - \delta \varepsilon/\varepsilon, \quad \delta D_{\omega}/D_{\omega} = \delta k/k \right]$ $\lambda_2 = C_{\omega_1} \omega^2 \left(\frac{P}{\varepsilon} - \beta_2^* \right) + D_{\omega}, \quad \delta \left(\frac{\lambda_2}{k} \right) = \frac{C_{\omega_1}}{L^2} (\beta_2^* - 1) \left[\frac{\delta L^2}{L^2} - \frac{\delta \beta_2^*}{\beta_2^* - 1} \right], \quad \int_{\beta}^{\beta_2^*} \frac{dx}{x-1} = \int_{L_{tot}^2}^{L^2} \frac{dy}{y}, \quad \frac{\beta_2^* - 1}{\beta - 1} = L_+^2$

Table 1. Minimal error $k - \omega$ models: both KOS and KOK hybridizations are considered in analysis options $\mathcal{O}_1, \mathcal{O}_2$ depending on v_t^* . Model errors λ , first variations, and resulting mode controls β^* are provided. Variations applied are given in brackets.

MINIMAL ERROR SIMULATION METHODS

Incompressible flow is considered for simplicity, corresponding compressible formulations can be found elsewhere. The incompressible continuity equation $\partial \tilde{U}_i / \partial x_i = 0$ and momentum equation are considered,

$$\frac{D\tilde{U}_i}{Dt} = - \frac{\partial(\tilde{p}/\rho + 2k/3)}{\partial x_i} + 2 \frac{\partial(v + v_t)\tilde{S}_{ik}}{\partial x_k}. \quad (1)$$

Here, $D/Dt = \partial/\partial t + \tilde{U}_k \partial/\partial x_k$ denotes the filtered Lagrangian time derivative and the sum convention is used throughout this paper. \tilde{U}_i refers to the i^{th} component of the spatially filtered velocity. We have here the filtered pressure \tilde{p} , ρ is the constant mass density, k is the modeled energy, v is the constant kinematic viscosity, and $\tilde{S}_{ij} = (\partial \tilde{U}_i / \partial x_j + \partial \tilde{U}_j / \partial x_i) / 2$ is the rate-of-strain tensor. The modeled viscosity is given by $v_t = C_{\mu} k^{1/2} L$. Here, C_{μ} is a model parameter with standard value $C_{\mu} = 0.09$, and L is a characteristic length scale. L can be calculated in different ways using $L = k^{3/2} / \varepsilon = k^{1/2} \tau = k^{1/2} / \omega$, where the dissipation rate $\varepsilon = k / \tau$ of modeled kinetic energy, the dissipation time scale τ , and the turbulence frequency $\omega = 1 / \tau$ are involved.

The minimal error approach can be applied in conjunction with a variety of turbulence models. Table 1 shows its application in regard to the $k - \omega$ model. $P = v_t S^2$ is the production of k , where $S = (2\tilde{S}_{mn}\tilde{S}_{nm})^{1/2}$. We have here $C_{\omega_1} = 0.49$, and $\sigma_{\omega} = 1.8$. In RANS, β^* is considered to be constant. Here, β^* is considered to be an undetermined parameter that needs to be chosen to minimize the hybridization error. The abbreviations KOS and KOK refer to the consideration of the $k - \omega$ model where the hybridization is accomplished in the scale equation (involving β^* that needs to be determined) or k -equation (involving ψ_{β} that needs to be determined), respectively. Both approaches can provide equivalent results as long as the coefficient relation $\beta^* = 1 + \beta - \psi_{\beta}$ is taken into account. In regard to both KOS and KOK models there are two analysis options. Option \mathcal{O}_1 is an exact hybridization where total viscosities need to be applied in turbulent transport terms. Option \mathcal{O}_2 is an hybridization where the usual model viscosities are involved in turbulent transport terms; an approximation is involved by the neglect of substantial derivatives in regard to the model coefficient calculation.

The structure of CES methods differs significantly from popular RANS-LES methods due to the involvement of resolution indicators like $0 \leq L_+ \leq 1$ in model equations. The latter measures the degree of flow resolution. $L_+ = L / L_{tot}$ is

defined in similarity to the modeled-to-total kinetic energy ratio $k_+ = k / k_{tot}$, where L refers to the modeled length scale contribution and L_{tot} refers to the total length scale contribution. In particular, $L_+ \approx 1$ represents an almost completely modeled (RANS) regime, whereas $L_+ \approx 0$ represents an almost completely resolved (LES) regime. Most importantly, in contrast to usually applied hybrid RANS-LES the model is informed about the actual resolution in this way, and the model is able to respond to resolution variations implied by changes of the model coefficient β^* . For example, a higher resolution (L_+ becomes smaller) decreases β^* . Thus, there is less dissipation of ω , ω increases which decreases the model viscosity $v_t = C_{\mu} k / \omega$. To minimize the error of a hybrid method means, therefore, to minimize the uncontrolled coexistence of resolved and modeled motion seen in popular hybrid RANS-LES.

CES FUNCTIONALITY AND COST FEATURES

It is worth noting that the CES approach reveal essential differences to usually applied wall-resolved LES (WRLES), WMLES, and DES. WRLES requires the use sufficiently fine grids, and it is often unclear whether LES resolution requirements are satisfied. Hybrid RANS-LES like WMLES methods are known to depend on simulation settings, the use of different (equilibrium or nonequilibrium) wall models, definitions of regions where different models and grids are applied, different mesh distributions, and setup options to manage the information exchange between such different flow regions. DES depends similarly on simulation settings, the results depend on the concrete model applied and the definition of differently

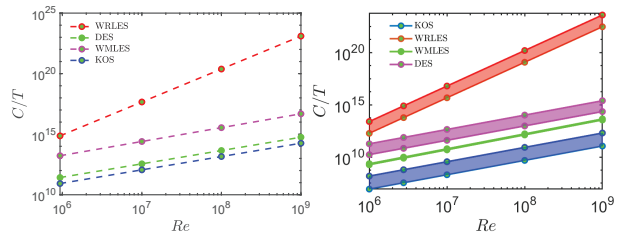


Figure 1. Cost scalings of CES vs. other methods: NASA wall-mounted hump flow (left) and the Bachalo & Johnson axisymmetric transonic bump flow (right).

treated simulation zones. Both DES and WMLES are known to depend on the mesh organization using the same number of grid points. In contrast, CES methods are independent of such functionality requirements, the model can be used as is. In particular, CES can be expected to enable reliable predictions under conditions where validation data are unavailable.

Also in regard to the computational cost of CES methods, there are essential differences to usually applied methods (Heinz *et al.*, 2020; Fagbade & Heinz, 2024a,b). The simulation cost are specified by $C = NN_t = TN/\Delta t$. Here, N is the number of grid points applied, N_t is number of time steps performed, $T = N_t\Delta t$ refers to the constant total physical simulation time, and Δt is the prescribed simulation time-step. N and Δt are known to vary with Re according to $N = \alpha_1 (Re/Re_0)^{\beta_1}$, $\Delta t = \alpha_2 (Re/Re_0)^{-\beta_2}$, where α_1 , α_2 , β_1 , and β_2 are constants (Heinz *et al.*, 2015; Mokhtarpoor *et al.*, 2016). Here, Re_0 is used as normalization. Implications of simulations of NASA wall-mounted hump flow and the Bachalo & Johnson axisymmetric transonic bump flow are presented in Fig. 1. As it may be seen, the simulation cost of CES are well below the cost of other methods, in particular, CES applications can be by orders of magnitude cheaper than other methods.

PERIODIC HILL FLOW SIMULATIONS

One of the applications of CES methods is the simulation of periodic hill flows as illustrated in Fig. 2 (Heinz *et al.*, 2020). This flow is a channel flow involving periodic restrictions. This flow, which is used a lot for the evaluation of turbulence models (Heinz, 2020), involves features such as separation, recirculation, and natural reattachment (Rapp & Manhart, 2011; Kähler *et al.*, 2016). A thorough evaluation of the performance of CES methods in regard to simulating periodic hill flows at the highest $Re = 37,000$ for which experimental data for model evaluation are still available can be found elsewhere (Heinz *et al.*, 2020). The CES-KOKU CES variant was applied (Heinz *et al.*, 2020).

An interesting question concerns the spatial uniformity of variations of the distribution of the resolution indicators L_+ , k_+ , and $\varepsilon_+ = \varepsilon/\varepsilon_{tot}$, which is certainly a desired feature to avoid imbalances of resolved and modeled motions. Fig. 3 demonstrates the ability of the hybrid model to produce almost uniform distributions of L_+ over most of the domain. The most noticeable deviation from this trend is given for $Re = 500K$ (G_{120}). Another question concerns the uniformity of resolution indicator variations in response to grid and Re variations. The question is whether there are indications of discontinuities in this regard, which would lead to questions about the applicability of CES methods for very high Re flows using rather coarse grids. The desired increase of variables like L_+ and k_+

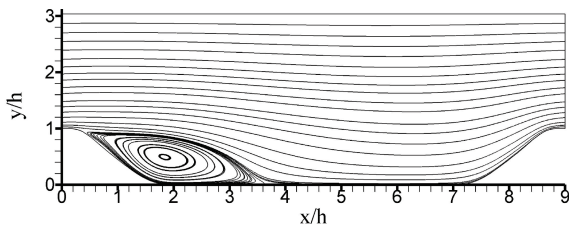


Figure 2. Velocity streamlines seen in periodic hill flows: results obtained by continuous eddy simulation at $Re = 37,000$. Reprinted with permission from Ref. (Heinz *et al.*, 2020). Copyright 2020 AIP Publishing.

due to coarser grids and increased Re requires a corresponding reduction of resolved motion (fluctuations), which requires a stable functioning of the fluctuation generation mechanism. Fig. 3 clearly demonstrates that there is a uniform response of L_+ to both grid coarsening and increased Re , including the near-wall region behavior (see, e.g., the insets showing profiles close to the lower wall in y_+ scaling).

A representative example of advantages is given in Fig. 4. The question about the asymptotic flow structure matters to our understanding to see whether there are asymptotically stable regimes of wall-bounded turbulent flows involving flow separation. This question relates to our understanding of which geometric conditions enable an asymptotically stable flow configuration (Heinz *et al.*, 2022), what is the corresponding concrete flow structure, and which Re are needed to accomplish an asymptotic flow structure. Figure 4 shows reattachment point predictions of experiments and CES results depending on Re . Available experimental results support the curve fit $0.49(Re/10^4)^{-1.4} + 3.71$ of Kähler *et al.* (2016). However, the availability of CES predictions reveals the unphysical behavior of this fit for high Re , it cannot be expected that the Re trend ends right after the available data range. The curve fit derived from CES predictions, $x_r = 3.23[1 + 15.1 \times 10^4/Re][1 + 0.5e^{-1.5 \times 10^{-4}Re}]/[1 + 12.4 \times 10^4/Re]$, provides a more plausible explanation of how the asymptotic Re regime is reached.

NASA HUMP FLOW SIMULATIONS

Seifert & Pack (2002) developed the wall-mounted hump model to investigate unsteady flow separation, reattachment, and flow control at a high Reynolds number $Re = c\rho_{ref}U_{ref}/\mu \approx 936K$ based on the chord length c and freestream velocity U_{ref} . Here, μ is the dynamic viscosity and the abbreviation *ref* indicates the reference freestream conditions, which are determined at the axial point $x/c = -2.14$. The model reflects the upper surface of a 20-thick Glauert-Goldschmied airfoil that was originally designed for flow control purposes in the early twentieth century. As a benchmark for comparison, we used the experiment conducted by Greenblatt *et al.* (Greenblatt *et al.*, 2006) without flow control. This benchmark case has been extensively documented on the NASA Langley Research Center's Turbulence Modeling Resource webpage and has been widely used for evaluating different turbulence modeling techniques, as discussed in the 2004 CFD Validation Workshop. We see in Figure 5 a strongly convex region just before the trailing edge, which induces flow separation.

A representative example of advantages is given in Fig. 6. This figure shows that that all methods involved in this comparison show a reasonable agreement with the experimental pressure coefficient profiles. The predictions from WRLES match the experimental measurement profile downstream and the model is capable of mimicking the dominant features of the flow. However, within the reattachment region, the second wall pressure peak is underpredicted by WRLES compared to CES-KOS and WMLES. Figure 6 also shows the mean skin friction coefficient obtained by CES-KOS, WMLES, and WRLES simulations, demonstrating their agreement with experimental values. In the separation zone, from $0 \leq x/c \leq 0.65$, WRLES underpredicts the skin friction coefficient, while WMLES overestimates the actual peak. In regard to post-reattachment, however, the C_f profiles of WRLES and CES-KOS match relatively well, despite using different frameworks, mesh sizes, and grid resolutions.

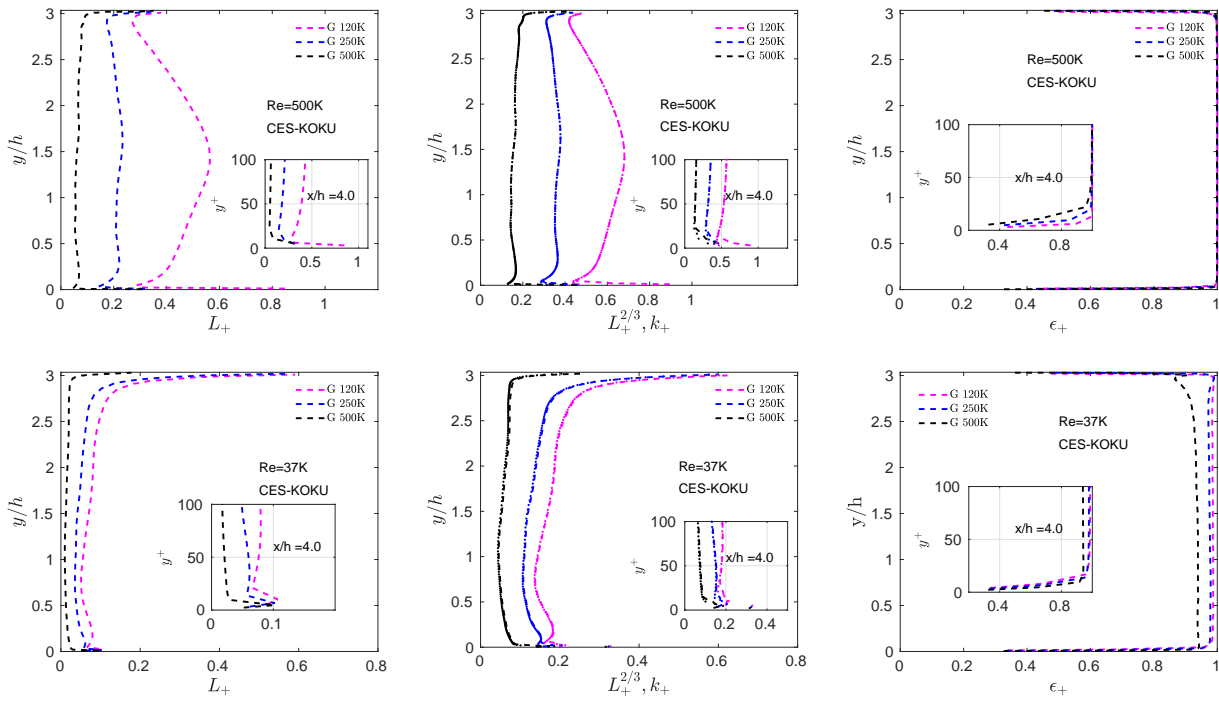


Figure 3. CES-KOKU results for the resolution indicators L_+ , k_+ , and ϵ_+ : Results are shown for $Re = 500K$ and $Re = 37K$, respectively, on G_{500} , G_{250} , G_{120} . The insets show profiles close to the lower wall in y_+ scaling. Reprinted with permission from Ref. (Heinz *et al.*, 2020). Copyright 2020 AIP Publishing.

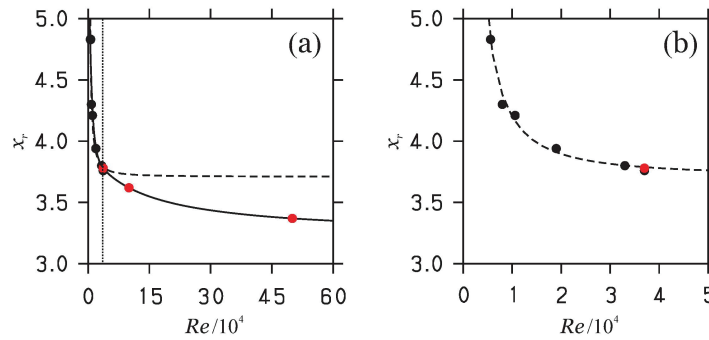


Figure 4. Reattachment point predictions x_r versus Re : experimental (black dots) (Rapp & Manhart, 2011; Kähler *et al.*, 2016) and CES results (red dots). The black line in (a) shows $x_r = 3.23[1 + 15.1 \times 10^4/Re][1 + 0.5e^{-1.5 \times 10^{-4}Re}]/[1 + 12.4 \times 10^4/Re]$, the dashed line shows $0.49(Re/10^4)^{-1.4} + 3.71$ of Kähler *et al.* (Kähler *et al.*, 2016). The vertical dotted line shows the range of previously available results. Figure (b) shows the zoomed-in curve fit of (Kähler *et al.*, 2016) compared to previous experimental and $Re = 37K$ CES results. Reprinted with permission from Ref. (Heinz *et al.*, 2020). Copyright 2020 AIP Publishing.

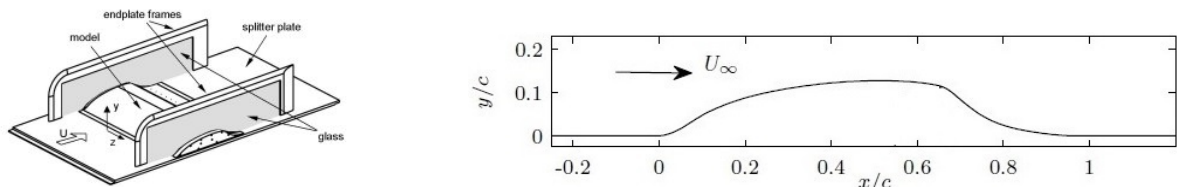


Figure 5. Wall-mounted hump geometry. Left: Experimental setup (Seifert & Pack, 2002); right: 2-D Computational layout.

BACHALO & JOHNSON AXISYMMETRIC TRANSONIC BUMP FLOW SIMULATIONS

Figure 7 shows a schematic diagram of the experimental configuration and the computational domain for the axisymmetric transonic bump considered (Bachalo & Johnson, 1986; Lynch *et al.*, 2020) along with the applied boundary conditions. This case pertains to shock-triggered boundary layer

separation induced by an axially-symmetric bump mounted on a slim spherical cylinder, which extends 61cm upstream. The case reflects the upper surface of a transonic wing. It is characterized by a Mach number (M_∞) of 0.875 and a Reynolds number (Re) of 2.763 M relative to the airfoil's chord length c .

Figure 8 shows in its first row streamwise velocity profiles obtained by CES-KOS, WMLES (Ren *et al.*, 2022) and WR-

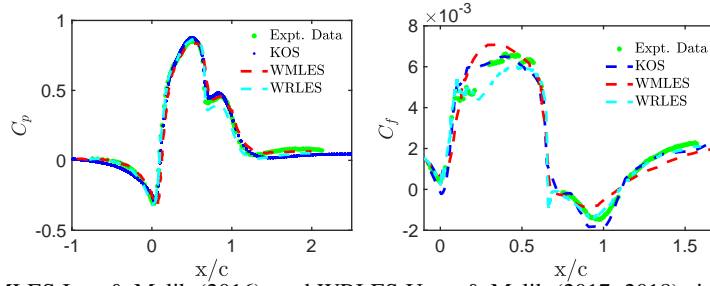


Figure 6. CES-KOS, WMLES Iyer & Malik (2016), and WRLES Uzun & Malik (2017, 2018) simulation results on the G_4 grid at $Re = 936K$: Pressure and skin-friction coefficients.

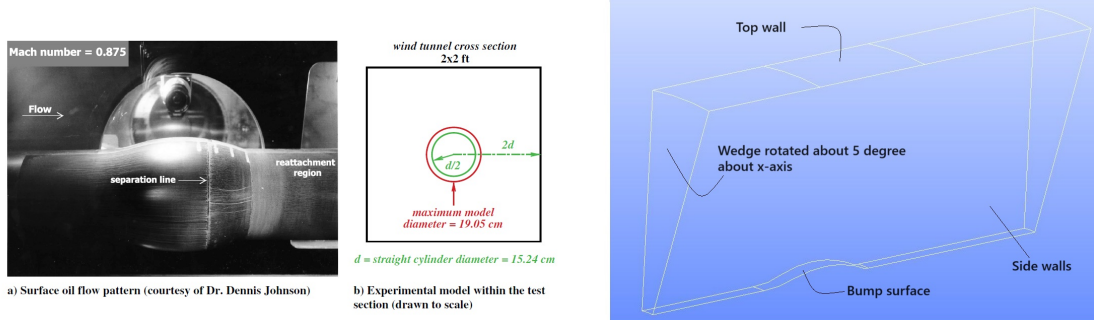


Figure 7. Axisymmetric transonic bump geometry: Experimental and computational configuration (Ren *et al.*, 2022; Uzun & Malik, 2019).

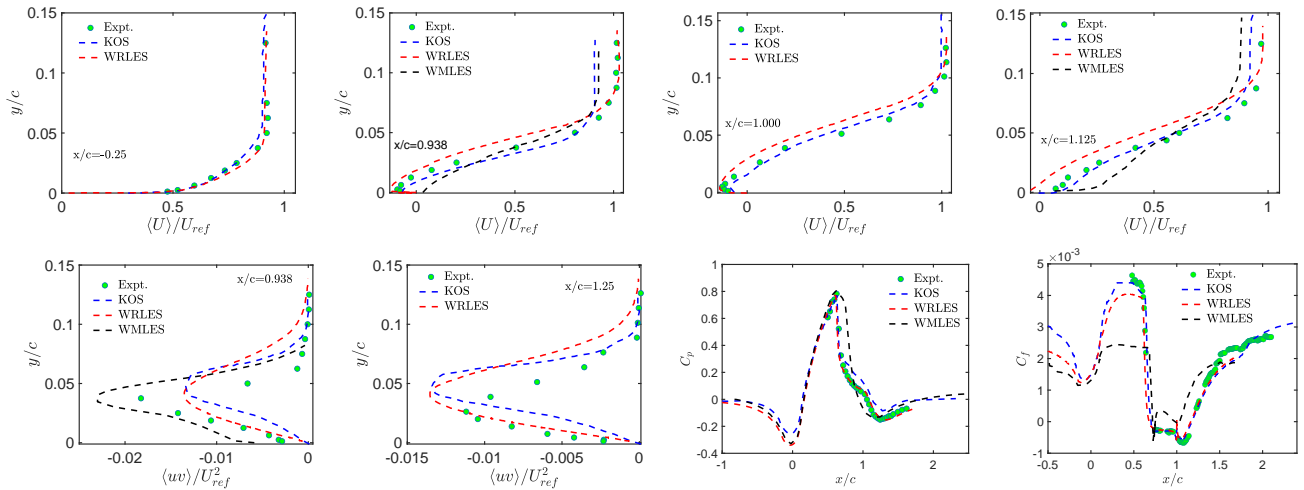


Figure 8. CES-KOS vs. LES-type WRLES (Uzun & Malik, 2019) and WMLES (Ren *et al.*, 2022) models: Profiles of the normalized streamwise velocity $\langle U \rangle / U_{ref}$, Reynolds stress $\langle uv \rangle / U_{ref}^2$, pressure and skin-friction coefficients at different locations.

LES (Uzun & Malik, 2019). It may be seen that the CES-KOS model predicts the streamwise velocity more accurately than WMLES and WRLES. In regard to turbulent shear stress profiles shown in the second row, we see a reasonable agreement of WMLES, WRLES, and CES-KOS with experimental data. It is of interest to note that CES-KOS and WRLES provide very similar results. In attached flow regions, WMLES overpredicts the turbulent shear stress. Due to its delayed reattachment point, WMLES predicts a faster separated shear layer growth and a higher maximum Reynolds stresses compared to CES-KOS. These trends have been noted in past numerical studies using alternative models (Sahu & Danberg, 1986).

Figure 8 also shows pressure coefficient distributions obtained by CES-KOS, WMLES, and WRLES. The figure helps to illustrate and validate the accuracy of CES-KOS predictions. The CES-KOS and WRLES models accurately predict pressure coefficient profiles due to their sufficient flow resolution

and ability. In contrast, WMLES predicts a linearly increasing pressure distribution within $x/c = (0.7, 1.1)$, it fails to accurately capture the separation zone. Furthermore, both CES-KOS and WRLES show reasonable predictions of the shock location and post-shock pressure recovery. The WRLES results agree slightly better with the experimental data downstream of the bump (between $x/c = 1.1$ and 1.3) compared to the CES-KOS model. Figure 8 also shows skin-friction coefficient distributions obtained by CES-KOS, WMLES, and WRLES. Evidently, WMLES significantly underestimates the skin-friction coefficient in the separation region and fails to accurately represent the post-separation flow physics. The predictions of CES-KOS and WRLES are very similar, with the exception that CES-KOS better agrees with the experimental data in the C_f plateau region upstream of separation. Overall, CES-KOS provides the most accurate predictions.

SUMMARY

The paper reports the advantages of CES methods, i.e. partially resolving simulation methods based on strict mathematics. Corresponding minimal error simulation methods include an essential mechanism that is missing in popular hybrid RANS-LES methods: the model integrates physics, it can dynamically respond to the actual amount of flow resolution, which is the essential mechanism to ensure a functional RANS-LES swing. This theoretical advantage relates to functionality features different from popular hybrid RANS-LES methods. WMLES and DES methods usually applied depend on a variety of simulations settings which are usually determined to maximize the simulation performance. In contrast CES methods do only depend on the details of the turbulence model applied but not on adjustable settings of the hybridization. In addition CES methods are computationally much more efficient than usually applied hybrid RANS-LES and WRLES.

Based on these advantages, CES methods were found to perform significantly better than DES and WMLES simulations and at least as good (or even better) than WRLES. The latter was shown for three complex flow applications: periodic hill flows at high Reynolds number (Heinz *et al.*, 2020), the NASA wall-mounted hump flow (Fagbade & Heinz, 2024b), and the Bachalo & Johnson axisymmetric transonic bump flow (Fagbade & Heinz, 2024a). An interesting overall observation of these applications was the fact that CES predictions are well balanced. This means the usual problem of DES, WMLES, and WRLES to perform well (not well) in regard to specific flow features (like velocities distributions, pressure and skin-friction distributions) was not observed in regard to CES predictions. Based on the stable functioning of CES methods, we discussed the asymptotic flow structure of the three flows considered at extreme Reynolds numbers.

We note that the use of CES methods as resolving LES is highly attractive to avoid the problem to involve the filter width as artificial (possibly unphysical) length scale. Similarly, the use of CES methods in almost RANS mode will relate to significant advantages because of the stable inclusion of unsteady turbulence.

REFERENCES

- Bachalo, W. D. & Johnson, D. A. 1986 Transonic, turbulent boundary-layer separation generated on an axisymmetric flow model. *AIAA J.* **24** (3), 437–443.
- Fagbade, A. & Heinz, S. 2024a Continuous eddy simulation (CES) of transonic shock-induced flow separation. *Appl. Sci.* **14** (7), 2705.
- Fagbade, A. & Heinz, S. 2024b Continuous eddy simulation vs. resolution-imposing simulation methods for turbulent flows. *Fluids* **9** (1), 22.
- Greenblatt, D., Paschal, K. B., Yao, C.-S. and Harris, J., Schaeffler, N. W. & Washburn, A. E. 2006 Experimental Investigation of Separation Control Part 1: Baseline and Steady Suction. *AIAA Journal* **44** (12), 2820–2830.
- Heinz, S. 2019 The large eddy simulation capability of Reynolds-averaged Navier-Stokes equations: Analytical results. *Phys. Fluids* **31** (2), 021702/1–021702/6.
- Heinz, S. 2020 A review of hybrid RANS-LES methods for turbulent flows: Concepts and applications. *Prog. Aerosp. Sci.* **114**, 100597/1–100597/25.
- Heinz, S. 2021 The continuous eddy simulation capability of velocity and scalar probability density function equations for turbulent flows. *Phys. Fluids* **33** (2), 025107/1–025107/13.
- Heinz, S. 2022 Minimal error partially resolving simulation methods for turbulent flows: A dynamic machine learning approach. *Phys. Fluids* **34** (5), 051705/1–051705/7.
- Heinz, S., Heinz, J. & Brant, J. A. 2022 Mass transport in membrane systems: Flow regime identification by Fourier analysis. *Fluids* **7** (12), 369.
- Heinz, S., Mokhtarpoor, R. & Stoellinger, M. K. 2020 Theory-based Reynolds-averaged Navier-Stokes equations with large eddy simulation capability for separated turbulent flow simulations. *Phys. Fluids* **32** (6), 065102/1–065102/20.
- Heinz, S., Stöllinger, M. & Gopalan, H. 2015 Unified RANS-LES simulations of turbulent swirling jets and channel flows. In *Progress in Hybrid RANS-LES Modelling (Notes on Numerical Fluid Mechanics and Multidisciplinary Design 130)*, pp. 265–275. Cham: Springer.
- Iyer, P. S. & Malik, M. R. 2016 Wall-modeled large eddy simulation of flow over a wallmounted hump. In *2016 AIAA Aerospace Sciences Meeting, AIAA SciTech Forum, AIAA Paper 16-3186*, pp. 1–22. Washington, D.C.
- Kähler, C. J., Scharnowski, S. & Cierpka, C. 2016 Highly resolved experimental results of the separated flow in a channel with streamwise periodic constrictions. *J. Fluid Mech.* **796**, 257–284.
- Larsson, J., Kawai, S., Bodart, J. & Bermejo-Moreno, I. 2016 Large eddy simulation with modeled wall-stress: recent progress and future directions. *Mech. Eng. Rev.* **3** (1), 15–00418/1–15–00418/23.
- Lynch, K. P., Lance, B., Lee, G. S., Naughton, J. W., Miller, N. E., Barone, M. F., Beresh, S. J., Spillers, R. & Soehnel, M. 2020 A CFD validation challenge for transonic, shock-induced separated flow: Experimental characterization. In *AIAA Scitech 2020 Forum, AIAA Paper 20-1309*, pp. 1–19.
- Menter, F., Hüppe, A., Matyushenko, A. & Kolmogorov, D. 2021 An overview of hybrid RANS–LES models developed for industrial CFD. *Applied Sciences* **11** (6), 2459.
- Mockett, C., Fuchs, M. & Thiele, F. 2012 Progress in DES for wall-modelled LES of complex internal flows. *Comput. Fluids* **65**, 44–55.
- Mokhtarpoor, R., Heinz, S. & Stoellinger, M. 2016 Dynamic unified RANS-LES simulations of high Reynolds number separated flows. *Phys. Fluids* **28** (9), 095101/1–095101/36.
- Rapp, C. & Manhart, M. 2011 Flow over periodic hills – an experimental study. *Exp. Fluids* **51**, 247–269.
- Ren, X., Su, H., Yu, H. H. & Yan, Z. 2022 Wall-modeled large eddy simulation and detached eddy simulation of wall-mounted separated flow via OpenFOAM. *Aerospace* **9** (759), 1–21.
- Sahu, J. & Danberg, J. 1986 Navier–Stokes computations of transonic flows with a two-equation turbulence model. *AIAA J.* **24**, 1744–1751.
- Seifert, A. & Pack, L. 2002 Active flow separation control on wall-mounted hump at high Reynolds numbers. *AIAA Journal* **40** (7), 1362–1372.
- Uzun, A. & Malik, M.R. 2018 Large-Eddy Simulation of flow over a wall-mounted hump with separation and reattachment. *AIAA Journal* **56** (2), 715–730.
- Uzun, Ali & Malik, Mujeeb R. 2017 Wall-resolved large-eddy simulation of flow separation over nasa wall-mounted hump. In *55th AIAA Aerospace Sciences Meeting*, pp. AIAA Paper 17–0538.
- Uzun, Ali & Malik, Mujeeb R. 2019 Wall-resolved large-eddy simulations of transonic shock-induced flow separation. *AIAA J.* **57** (5), 1955–1971.